Applied Catalysis B: Environment and Energy 383 (2026) 126037

Contents lists available at ScienceDirect

Applied Catalysis B: Environment and Energy

journal homepage: www.elsevier.com/locate/apcatb

Design of Ni-promoted $Ca_2Fe_2O_5$/modified ceria as oxygen carrier for fast and carbon-resistant chemical-looping steam methane reforming

Andrea Strazzolini [a], Juan Felipe Basbus [b,1], Carla de Leitenburg [a], Jordi Llorca [c], Marta Boaro [a,*], Alessandro Trovarelli [a]

[a] Polytechnic Department, University of Udine and INSTM, Via del Cotonificio 108, Udine 33100, Italy
[b] Department of Civil, Chemical and Environmental Engineering (DICCA), University of Genova (UniGe), Via Alla Opera Pia 15, Genoa 16145, Italy
[c] Institute of Energy Technologies, Department of Chemical Engineering and Center for Research in Multiscale Science and Engineering, Universitat Politècnica de Catalunya, EEBE, Eduard Maristany 10-14, Barcelona 08019, Spain

ARTICLE INFO

Keywords:
Chemical looping
Steam methane reforming
$Ca_2Fe_2O_5$
Carrier oxides
Catalytic promotion
Composite oxides
Modified ceria

ABSTRACT

Chemical looping steam methane reforming enables the production of high-purity syngas and hydrogen while eliminating the energy-intensive downstream separation steps typically required by conventional technologies. $Ca_2Fe_2O_5$ is a promising oxygen carrier thanks to its high redox stability and low equilibrium pO_2. However, its practical application is hindered by sluggish reduction kinetics. Here, we have overcome this limitation by preparing nickel-promoted composite oxygen carriers (OC) through the physical mixing of $Ca_2Fe_2O_5$ and modified CeO_2. The selective deposition of Ni on the surface of the CeO_2-based phase significantly increases the OC reduction rate, outperforming samples in which Ni is in close contact with $Ca_2Fe_2O_5$ (either on the surface or within the lattice). SiO_2 modified ceria was found to be more effective than CeO_2-Al_2O_3 and $Ce_{0.8}Zr_{0.2}O_2$ in promoting the microstructural stability of CeO_2 within the composite, ensuring consistent performance over multiple redox cycles. The co-presence of $Ca_2Fe_2O_5$ and the catalyst in the same reactive bed effectively limits carbon formation at a low OC conversion degree. *In situ* synchrotron X-ray diffraction and isothermal packed-bed tests revealed a gas-mediated synergistic mechanism whereby carbon deposition was inhibited by H_2O and CO_2 generated locally from the reduction of $Ca_2Fe_2O_5$. This led to fast oxygen exchange and stable syngas production. After 50 reaction cycles, the composite OC produced 13.0 mmol/g of syngas in the reduction step with 88 % CH_4 conversion, and 6.8 mmol/g of H_2 in the water splitting step with > 99 % purity, demonstrating the potential of this OC design strategy.

1. Introduction

Fossil fuels are currently the dominant global source of energy, with projections indicating that their share will remain above 60 % in 2050 [1]. Considering the forecasted increase in the total energy demand, there is a growing need for efficient conversion technologies, particularly when it comes to non-renewable resources. Presently, natural gas reforming represents the major source of H_2 and syngas, [2,3], which in turn are key intermediates in industrial chemical synthesis. Chemical Looping Steam Methane Reforming (CL-SMR) has been recently considered as an alternative to conventional Steam Methane Reforming (SMR), since it can provide a viable process intensification approach with inherent gas-gas separation [4]. Chemical Looping (CL) is a process strategy in which a given reaction is decomposed into multiple sub-reactions separated in time (in a dynamically operated reactor) [5] or space (in multiple interconnected reactors) [6]. The sub-reactions are connected by a chemical intermediate, typically a solid, that cyclically alternates between the reacted and regenerated states. When applied to SMR, CL utilizes a circulating metal oxide-based oxygen carrier capable to selectively oxidise CH_4 to CO and H_2 through the release of its lattice oxygen (reduction step), and to recover the original state by oxidation with steam, thus producing a stream of pure H_2 (oxidation step). The availability of suitable Oxygen Carriers (OC) is crucial for the commercial-scale deployment of CL-SMR processes. The choice of the

* Corresponding author.
E-mail address: marta.boaro@uniud.it (M. Boaro).
[1] Present address: Aragon Nanoscience and Materials Institute (INMA), Higher Council for Scientific Research (CSIC), University of Zaragoza (UniZar) and Condensed Matter Physics Department, C/Pedro Cerbuna 12, 50009 Zaragoza, Spain.

https://doi.org/10.1016/j.apcatb.2025.126037
Received 1 August 2025; Received in revised form 28 September 2025; Accepted 1 October 2025
Available online 1 October 2025

oxygen carrier strongly influences fuel conversion and selectivity during the reduction step, as well as steam conversion in the oxidizer. Additionally, it determines the operative conditions and significantly impacts the overall economics of the process. The scientific community has invested significant effort in developing OCs able to meet the stringent requirements of CL processes, such as high oxygen transfer capacity (OTC), good mechanical and chemical stability, good recyclability, low cost, and a low environmental footprint [7]. In this framework, Fe-based oxygen carriers are particularly attractive thanks to their environmental friendliness, large natural abundance, low cost, high OTC and suitable thermodynamics [8]. However, iron oxide-based OCs face several challenges, such as relatively low reactivity with CH_4 compared to other transition metal oxides, their tendency to agglomerate at high reduction degrees and their non-optimal selectivity to partial oxidation products [9]. Multiple strategies have been proposed to address these challenges, such as the introduction of structural and chemical promoters and the confinement of iron into complex oxides such as perovskites and garnets [10–16]. $Ca_2Fe_2O_5$ (C2F) is a brownmillerite-type oxide that has recently been considered as OC for CL-SMR, thanks to its superior stability in redox cycles, its low equilibrium oxygen partial pressure (pO_2) and its fast oxygen ion transport [15,17]. Despite the favourable properties, it suffers from slow reduction kinetics [9], thus negatively affecting the CH_4 conversion and the specific syngas and H_2 yields. Different strategies have been proposed and evaluated to improve C2F performance in chemical looping schemes. Studies reported that the introduction of a support material is beneficial to improve the reduction kinetics with CH_4 because it increases dispersion of the active phase [18]. When a redox-active CeO_2-based material is used as a support, a composite OC with a higher reactivity than the linear superposition of the reactivities of the single components can be obtained, indicating the existence of a certain degree of synergy between the two materials [19]. Another effective approach to boost the reactivity of C2F involves doping with transition metals (e.g., Ni, Cu) that are known to activate CH_4. This strategy significantly increases the feed conversion rate. However, it raises concerns about the stability of the OC due to the formation of segregated phases following prolonged redox cycling [20]. Recent density functional theory (DFT) calculations highlighted the complex effects of metal doping. On one hand, doping lowers the energy required for surface oxygen vacancies (V_{Os}) formation, enhancing redox capabilities. On the other hand, reducing the total V_{Os} energy increases the energy input required for H_2O splitting and H_2 formation [21].

An alternative strategy involves introducing metal catalysts separately from the OC. It was reported that a simple physical mixture of a FeO_x/CeO_2 OC and a relatively low amount of Ni/CeO_2 catalyst can significantly enhance fuel conversion in chemical looping combustion and reforming applications [22,23]. However, placing a barrier between the C2F phase and the Ni-based catalyst, while preventing undesired phase formation, can also hinder oxygen supply from the OC to the catalyst. This limitation impairs the removal of solid carbon deposits from catalyst active sites by oxidation [24], potentially causing catalyst deactivation due to coke formation and reducing H_2 purity during the steam oxidation step due to CO evolution from carbon gasification with H_2O.

Here we pioneer a dual-lever strategy that couples tailored catalytic functionalisation with the engineered synergy of complementary oxygen carriers. Starting with an ancillary Zr-doped CeO_2 phase, we benchmark three Ni incorporation routes to identify the configuration that best combines CH_4 activation with cyclic stability: (i) substitution within, (ii) deposition onto, and (iii) deposition alongside C2F. The study was then extended to other promoting substituents in ceria, namely Al_2O_3 and SiO_2, with the goal of ascertaining the role of CeO_2 structural promoters and maximizing the OC stability. In situ synchrotron XRD and reactivity tests provided valuable insights for the optimisation of Ni-lean, CeO_2-supported composites, furnishing design guidelines for durable, low-cost CL-SMR oxygen carriers. This integrated approach enables the identification of $Ca_2Fe_2O_5$-SiO_2-modified CeO_2 (10 % mol.) as a suitable formulation, offering superior stability and durability, as well as a higher degree of Ni-support interaction, coupled with a more effective regeneration strategy. It overcomes the kinetic limitations previously reported for C2F, enabling near-quantitative CH_4 conversion, sustained redox stability and hydrogen purities above 99 %.

2. Methods

2.1. Materials

$Ca_2Fe_2O_5$ (C2F) was synthesized by the coprecipitation method, following the procedure reported in [25]. 1 M solutions of Fe $(NO_3)_3$•9 H_2O (Treibacher Industrie A.G.) and $Ca(NO_3)_2$•4 H_2O (Sigma Aldrich) were prepared and mixed in equal amounts. The mixture was stirred at room temperature for 20 min. Thereafter, a 0.5 M NaOH (VWR Chemicals) and 0.5 M $NaCO_3$ (Carlo Erba) solution was added dropwise under vigorous stirring until reaching a pH of 12.5. The slurry was aged under constant stirring for 6 h at room temperature and then filtered and washed four times with demineralized water. The cake was dried at 100 °C for 12 h and calcined at 1150 °C (heating rate: 10 °C/min) in a dry air flow for 6 h.

Ni-doped C2F ($Ca_2Fe_{1.95}Ni_{0.05}O_5$) was synthesized via a modified Pechini method, following the procedure reported in [20]. 1 M solutions of $Fe(NO_3)_3$ 9 H_2O (Treibacher Industrie A.G.), $Ca(NO_3)_2$ •4 H_2O (Sigma Aldrich) and $Ni(NO_3)_2$•6 H_2O (VWR chemicals) were prepared and mixed according to the desired stoichiometry. The solution was stirred at ambient temperature for 20 min. Then citric acid (Sigma Aldrich) and ethylene glycol (VWR Chemicals) were added to obtain citric acid:metal ion and ethylene glycol:citric acid molar ratios of 1. The obtained solution was kept at 60 °C for 2 h under constant stirring. The obtained gel was then dried for 12 h at 220 °C, and successively calcined at 950 °C for 3 h, using a ramp rate of 5 °C/min.

Commercial CeO_2 powder was provided from Rhodia S.A. $Ce_{0.8}Zr_{0.2}O_2$ and CeO_2-Al_2O_3 (10 % mol. Al_2O_3) were prepared by coprecipitation, modifying the procedure described in [26]. Briefly, stoichiometric amounts of $Ce(NO_3)_3$·6 H_2O salt (Treibacher Industrie AG) and either $ZrO(NO_3)_2$ liquid gel (Treibacher Industrie AG) or Al $(NO_3)_3$·9 H_2O salt (Sigma Aldrich) were dissolved in demineralized water obtaining a 0.2 M solution. The solution was then stirred for 15 min, thereafter concentrated H_2O_2 (35 %, Sigma-Aldrich) was added to obtain a $[H_2O_2]$/[total metals ions] molar ratio equal to 3. After 45 min of continuous stirring at room temperature, concentrated NH_3 solution (28 %wt. Sigma-Aldrich) was added dropwise to obtain a pH value of 10.5. The precipitate was maintained under continuous stirring for 4 h, then filtered and washed three times with demineralized water, and the resulting cake was dried at 100 °C overnight. The dry precipitate was calcined in air at 500 °C for 4 h.

CeO_2-SiO_2 (10 % mol. SiO_2) was prepared by coprecipitation, following a procedure adapted from [27]. Stoichiometric amounts of Ce $(NO_3)_3$·6 H_2O salt (Treibacher Industrie AG) and tetraethyl orthosilicate (TEOS, Sigma Aldrich) were dissolved in anhydrous Ethanol (Sigma Aldrich). After 2 h of continuous stirring at room temperature, an excess of concentrated NH_3·solution (28 % Sigma-Aldrich) was quickly added to the solution. The precipitate was maintained under stirring for 2 h at 60 °C and then dried at 100 °C overnight. The dry precipitate was calcined in air at 500 °C for 3 h.

All CeO_2-based materials underwent a further calcination step at 850 °C for 3 h.

Ni was loaded onto supports with a Ni/support weight ratio of 1.06 %, (unless otherwise specified) using the incipient wetness impregnation method; $Ni(NO_3)_2$·6 H_2O (Sigma-Aldrich) was used as the precursor. After impregnation, the samples were dried at 100 °C overnight and then calcined at 500 °C for 1 h.

2.2. Ex situ characterization

X-Ray diffraction patterns were collected on a Philips X'Pert equipment with an X'Celerator detector, using Cu Kα radiation and operating at 40 kV and 40 mA, with a step size of 0.02° and 40 s per step.

N_2 adsorption–desorption isotherms were obtained at −196 °C using a Micromeritics Tristar apparatus. The surface area was calculated by the Brunauer–Emmett–Teller (BET) method. The pore size distribution was calculated by the Barrett-Joyner-Halenda (BJH) method from the desorption branch of the isotherm. The total pore volume was calculated from the maximum adsorption point at relative pressure $p/p^\circ = 0.99$. Prior to the N_2 adsorption, the samples were heated in vacuum at 150 °C for 1.5 h.

Thermogravimetric analysis (TGA) was carried out in a TA instruments Q500 analyser. Approximately 15 mg of powdered sample were loaded into a platinum pan. Prior to the analysis, samples were held at 500 °C in pure N_2 to remove physisorbed species. Reductions were performed using a 5 % H_2 (balance N_2) atmosphere, with a constant gas flow of 60 ml/min. The sample was heated from 100 to 850 °C with a heating rate of 10 °C/min and held at the maximum temperature for 30 min. The reduction kinetics of composite samples with CH_4 was investigated in a Netzsch STA 2500 Regulus apparatus. Approximately 15 mg of powdered sample were loaded in an alumina pan and heated to 800 °C (ramp 10 °C/min) in pure N_2 and then exposed to 5 % CH_4 in N_2 (100 ml/min) for 20 min.

The reduction of as-prepared and Ni-loaded modified CeO_2 samples was investigated performing Temperature-Programmed Reductions (TPR) in a Autochem II 2920 Micromeritics apparatus. 50 mg of powdered sample were loaded and heated to the target temperature with a constant heating rate of (10 °C/min) under a gas flow of 5 % H_2 in N_2 (35 ml/min). Prior to the analysis, samples were held at 350 °C in pure N_2 to remove physisorbed species.

Scanning Electron Microscopy (SEM) images were acquired with a JEOL JSM7610F Plus Field Emission Gun (FEG) instrument, equipped with an energy-dispersive X-ray spectroscopy (EDS) analyser. Prior to the analysis, the powders were ultrasonically dispersed in ethanol and deposited onto a gold-coated brass sample holder.

Microstructural characterization by high-angle annular dark-field scanning transmission electron microscopy (HAADF-STEM) images and EDS was carried out on a ThermoFisher Scientific Spectra 300 monochromated instrument with double aberration correction operating at an accelerating voltage of 200 kV. Prior to the analysis, samples were dispersed in ethanol and deposited onto a lacey carbon copper grid.

2.3. Microreactor setup and chemical looping tests

CH_4-TPRs, isothermal CH_4 reduction and CL-SMR tests were performed in a custom-built laboratory setup. A schematic representation of the setup is provided in Figure S1. The setup includes a gas feeding system consisting of five mass flow controllers (Brooks Instruments). Steam was introduced by flowing helium through a jacketed saturator maintained at a constant temperature of 50 °C. To prevent steam condensation, all gas lines leading to and from the reactor were heated. Powdered samples were placed inside a quartz reactor (8 mm internal diameter), positioned within an electrically heated furnace. A K-type thermocouple, located approximately 5 mm above the sample, was used to continuously monitor the sample temperature. The reactor outlet was connected to a calibrated mass spectrometer (Hiden Analytical HPR20). Calibration factors for CH_4, H_2, CO, CO_2, and O_2 were regularly updated using certified gas mixtures. The calibration factor for H_2O was determined based on the amount of H_2 consumed during the reduction of a known quantity of CuO. System accuracy was verified through carbon balance calculations, closed to within 10 %.

For CH_4-TPR experiments, 50 mg of sample were loaded into the reactor and pretreated by heating to 500 °C for 30 min in pure He to remove physisorbed species. Subsequently, the samples were heated from 100 °C to 880 °C (10 °C/min) under a flow of 10 % CH_4 in He. After the experiment, all samples were reoxidized (20 min in 10 % H_2O followed by 10 min in 5 % O_2) and cooled to room temperature for XRD analysis. Throughout the test, the total gas flow rate was maintained at 50 ml/min.

Isothermal CH_4 reduction and CL-SMR experiments were run at 800 °C. The test procedure is reported in Figure S2. For each experiment, 200 mg of sample were loaded in the microreactor and heated up to reaction temperature in pure He. CL-SMR cycles consisted of three sequential steps: (i) reduction with 10 % CH_4 (5.5 min), (ii) steam oxidation with 10 % H_2O (11 min) and (iii) oxygen oxidation with 5 % O_2 (3 min). This final step was included to ensure complete reoxidation of the sample and the full removal and quantification of any solid carbon deposits formed during the cycle. An extended reduction time of 45 min was used for the $Ca_2Fe_2O_5$ sample to take in account its low reactivity toward CH_4. The inlet flow rate was kept constant at 50 Nml/min, obtaining a GHSV ≈ 20.000 h^{-1}.

The fuel conversion during the reduction step was calculated as:

$$X_{CH_4} = 1 - \frac{n_{CH_4,OUT}}{n_{CH_4,IN}} \quad (1)$$

The syngas selectivity was calculated as:

$$S_{syngas} = \frac{n_{H_2} + n_{CO}}{n_{H_2} + n_{CO} + n_{H_2O} + n_{CO_2}} \quad (2)$$

The H_2 purity, referred to the steam oxidation step, was calculated as:

$$S_{H_2} = \frac{n_{H_2}}{n_{H_2} + n_{CO} + n_{CO_2}} \quad (3)$$

2.4. In-situ time-resolved XRD

Synchrotron XRD experiments were performed at the BL04 beamline Materials Science and Power Diffraction (MSPD) beamline of ALBA synchrotron (Barcelona, Spain). This beamline was operated at 30 keV (wavelength equal to 0.4139 Å) in transmission mode (Debye-Scherrer geometry). Diffraction patterns were collected every 15 s with a MYTHEN-II detector over a 2θ range of 0.55° to 60°. CL-SMR cycles were performed with a 2-minute He purge between each step and included: (i) a 7-minute reduction in 2.5 % CH_4 in He, (ii) a 6-minute oxidation in 10 % CO_2 in He, and (iii) a 3-minute oxidation in 20 % O_2 in He. The sample underwent a total of 14 full cycles, with the final four alternating between CO_2-only or O_2-only oxidation steps and standard cycles. When a single oxidant was used, the oxidation step was extended to 7 min.

3. Results and discussion

Here we report the design and evaluation of an advanced composite OC for chemical-looping steam methane reforming (CL-SMR). The formulation couples (i) C2F, selected for its high oxygen-transfer capacity, low cost and redox stability; (ii) a CeO_2-based secondary OC that enhances the reducibility of C2F; and (iii) catalytic amounts of Ni to promote CH_4 activation. We first benchmark three Ni-placement strategies (lattice doping of C2F, surface impregnation of C2F, and selective impregnation of Zr-doped CeO_2) to establish how promoter location governs redox properties, reactivity and durability. The choice of a Zr-doped CeO_2 as reference grounds on previous studies [19]. Next, we screen modified CeO_2 supports to maximise stability while minimising Ni usage. Finally, comprehensive structural and kinetic analyses elucidate the factors that control performance and reveal the synergistic interactions among the composite's constituents.

3.1. Ni deposition: redox characterization of promoted OCs

Figure S3 reports the X-ray diffractograms of pure and Ni-modified

C2F. No crystalline phases other than $Ca_2Fe_2O_5$ were detected, indicating the effective dispersion of Ni in the impregnated sample and the successful substitution of Ni into the C2F lattice in the doped sample. The latter observation is further evidenced by a slight shift of the C2F diffraction peaks towards higher angles, attributable to the larger ionic radius of Ni^{2+} compared to Fe^{3+}[28].

Temperature-programmed reduction studies allowed to elucidate how Ni alters the redox behaviour of C2F and CZ samples. Fig. 1 shows the thermogravimetric analyses carried in H_2. Pure C2F reduction proceeds at a very slow pace starting from 550 °C and becomes significantly more pronounced above 750 °C (Fig. 1a), as noted in previous reports [29]. The Ni-impregnated sample exhibits a weight loss between 520 and 580 °C, corresponding to 2.2 % of the total mass. This loss cannot be attributed solely to the reduction of NiO to Ni, which, based on the nominal Ni content, would account for a 0.22 % decrease. This suggests that Ni promotes the reduction of C2F, likely involving superficial regions or areas in close contact with Ni particles [30,31]. A second weight loss is observed from 750 °C, matching the high-temperature behaviour of the unmodified C2F. The Ni-doped C2F begins its reduction at 650°C and progresses to completion by 865 °C. Experimental studies and Density Functional Theory (DFT) simulations indicate that substituting Fe^{3+} with Ni^{2+} induces lattice distortions in C2F, which in turn lower the formation energy of oxygen vacancies and reduce the energy barrier for lattice oxygen diffusion [21,32], allowing a faster oxygen exchange. Pure CZ reduction begins at lower temperatures than C2F, as reported in Fig. 1b. An initial weight loss between 460 and 620 °C is observed, associated with the reduction of surface Ce^{4+} species, followed by a partially overlapping second event extending up to 900 °C, attributed to the reduction of bulk Ce^{4+} cations [33]. In the Ni-promoted CZ sample, an initial weight loss is observed at lower temperatures (250–450 °C). The observation is attributed to the reduction of Ni species interacting with the CeO_2 surface with varying strength, as well as the facilitated reduction of surface Ce^{4+} cations via hydrogen spillover from neighbouring Ni sites [34,35].

Fig. 2 reports CH_4 consumption profiles of the C2F-based samples during CH_4-TPRs tests. Pure C2F (Fig. 2a) is not reactive with CH_4 below 800 °C. The oxygen exchange rate increases steadily until the maximum temperature is reached. After reaching the maximum temperature, the evolution of oxygen-containing gases ceases abruptly, and only H_2 is produced via CH_4 pyrolysis. The impregnated sample (Fig. 2b) starts reacting with CH_4 at a much lower temperature. A sharp increase in H_2 and CO concentrations is observed at 490 °C, associated to the reduction of NiO particles present on the surface to metallic Ni. This is followed by a progressive increase in H_2 and CO production up to 660 °C, beyond which CO levels drop rapidly and mainly H_2 is detected. The doped sample (Fig. 2c) exhibits behaviour similar to that of undoped C2F but shifted to lower temperatures: the reaction begins at 660 °C, and oxygen exchange terminates before reaching the maximum temperature. By quantifying the amount of lattice oxygen exchanged before the onset of extensive methane cracking it becomes evident that the presence of Ni limits the oxygen exchange capacity prior to carbon formation. To provide a quantitative description of the phenomenon, the carbon formation threshold was arbitrarily defined as the point where the H_2/CO ratio exceeds 5. The exchanged lattice oxygen decreases from 10.6 mmol/g for pure C2F to 7.1 and 7.7 mmol/g for the Ni-impregnated and Ni-doped samples, respectively. This quantity is calculated according to Eq. (4), where $\Delta n^*_{[O]}$ is the amount of lattice oxygen exchanged per gram of samples, W is the sample weight and $\dot{n}_i$ represents the molar flow rate of species i at the reactor outlet.

The diffraction patterns of the samples before and after the test are reported in Figure S4. Both the Ni-modified samples show the presence of segregated phases, identified as spinel $NiFe_2O_4$ for the impregnated sample and both $NiFe_2O_4$ and NiO for the doped sample. These mixed phases were reported to reduce the number of accessible Ni active sites, thereby decreasing the oxygen carrier performance [20,36].

$$\begin{aligned} \Delta n^*_{[O]} &= \frac{1}{W}\int_0^{t^*} (\dot{n}_{H_2O} + \dot{n}_{CO} + 2 \quad \dot{n}_{CO_2})dt \\ t^* &= \min\left\{ t \in [0, \quad t_{fin}] \quad | \quad \frac{\dot{n}_{H_2}}{\dot{n}_{CO}} < 5 \right\} \end{aligned} \tag{4}$$

Figure S5 shows the CH_4-TPR profiles of pure and impregnated CZ. In this case as well, the addition of Ni enhances the oxygen exchange at low temperature. Nevertheless, as soon as metallic Ni is produced a very high selectivity towards CH_4 pyrolysis is obtained.

To conclude, Nickel promotes low-temperature CH_4 activation and lattice oxygen exchange in both C2F and CZ. However, the two hosts, respond differently in terms of products selectivity, depending on the oxygen transfer rate from the host to the catalytically active sites.

3.2. Comparative assessment of Ni promoted OCs composites

The reactivity of the composite OC materials in Table 1 was assessed via isothermal reduction in a TGA, using 5 % CH_4 in He as the reducing gas (Fig. 3a). All Ni-containing samples exhibited a faster weight loss compared to the reference C2F-CZ sample, indicating enhanced reduction kinetics. However, the rate depended on where Ni was located. In the impC2F-CZ and dopC2F-CZ samples, where Ni is incorporated respectively on the surface of C2F and into the bulk, the reduction rate was lower than in the C2F-impCZ sample, in which Ni is selectively impregnated on the CZ phase only. In this latter configuration, chemical interactions between C2F and Ni are minimized. Conversely, in impregnated and doped C2F, the formation of Ni–Fe alloys or mixed oxides may occur, as observed after the CH_4-TPR.

These results corroborate the trends obtained during CL-SMR tests (Fig. 3b). The C2F-impCZ sample achieved near-complete fuel conversion in the first cycle, significantly outperforming the other samples, for

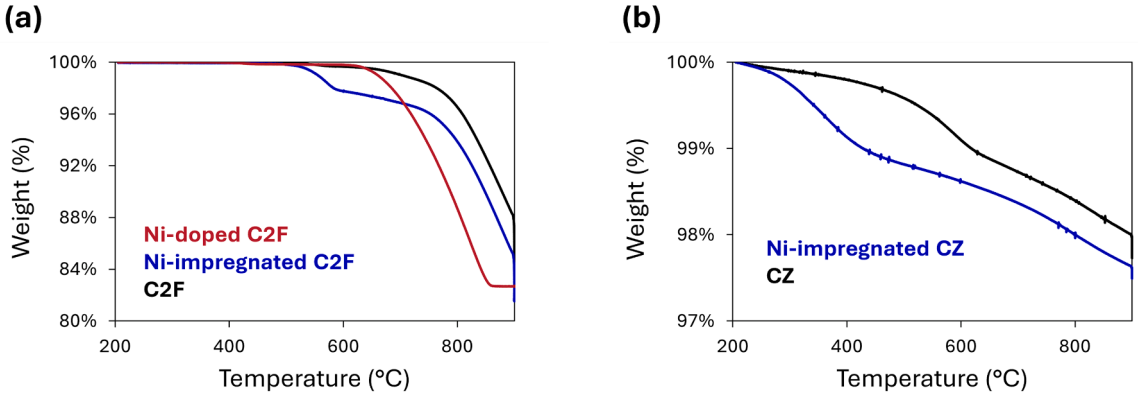

Fig. 1. TGA curves of (a) C2F and Ni-modified C2F and (b) CZ and Ni-modified CZ in a 5 %-H_2-N_2 flow.

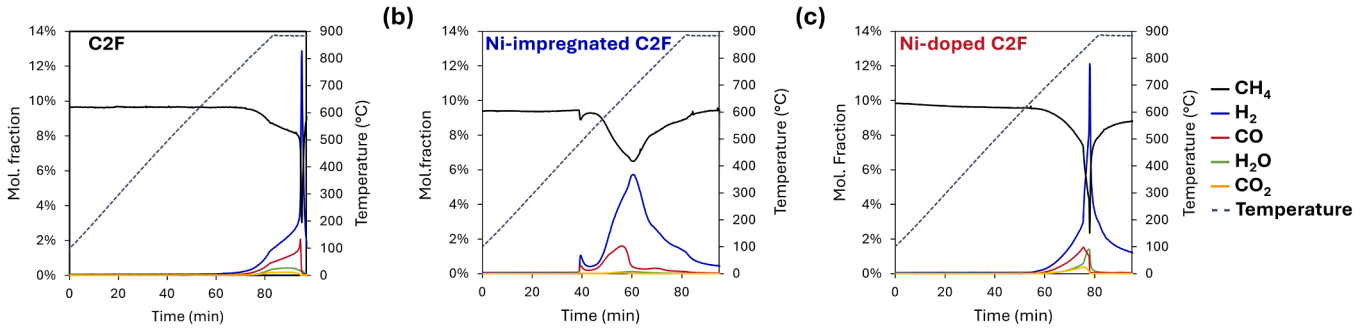

Fig. 2. CH_4-TPR of (a) C2F, (b) Ni-impregnated C2F and (c) Ni-doped C2F.

Table 1
Composition and sample label of the prepared composite OCs.

Sample ID	C2F-based component (50 % wt.)	CZ-based component (50 % wt.)
C2F-CZ (reference)	C2F	CZ
impC2F-CZ	Ni-impregnated C2F (1.06 wt %)	CZ
dopC2F-CZ	$Ca_2Fe_{1.95}Ni_{0.05}O_5$	CZ
C2F-impCZ	C2F	Ni-impregnated CZ (1.06 wt %)

which CH_4 conversion remained below 20 %. While all samples experienced a decrease in CH_4 conversion over successive cycles, the drop was particularly sharp for C2F-impCZ, from 95 % in the first cycle to 30 % after ten cycles, stabilizing afterwards. X-ray diffraction analysis on tested specimens revealed the presence of minor amounts of segregated phases, such as CaO and Fe_2O_3, with no crystalline Ni-containing compounds detected within the instrument's sensitivity range (Figure S6).

The advantages and limitations of blending C2F with Ni-impregnated CZ are more clearly illustrated by comparing the isothermal reduction profiles in 10 % CH_4 and the corresponding outlet gas composition for the individual components and their mixture, as shown in Fig. 4. Pure C2F exhibits a relatively low CH_4 conversion, which gradually improves with the extent of reduction and successive redox cycles, in agreement with previous studies [29]. This progressive increase in reactivity is attributed to the formation of catalytically active metallic iron during reduction, as well as to morphological changes in the C2F structure induced by repeated redox cycling [37,38]. Conversely, Ni-impregnated CZ achieves near-complete conversion at the beginning of the reduction. After about one minute of exposure, conversion drops sharply. At this point, the pyrolysis reaction becomes predominant (as evidenced by the increase of the H_2/CO ratio, shown in Fig. 4d) and likely deactivates the OC. A modest decline in CH_4 conversion is observed over successive cycles. Notably, the blended oxygen carrier effectively converts most of the CH_4 feed with high selectivity to H_2 and CO. However, the high conversion level observed during the first cycle is not maintained in subsequent cycles.

In short, TGA and CL-SMR results demonstrate that using an ancillary Ce-based oxygen carrier to host Ni is an effective way to enhance the redox properties of C2F. In absence of a physical barrier between the catalyst and C2F, $NiFe_2O_4$/NiO domains reduce the number of active sites. However, the significant decrease in activity in the C2F-impCZ configuration suggests that the long-term performance of such a composite primarily depends on the stability of Ni nanoparticles, deemed responsible for the high CH_4 conversion.

3.3. Selection of other Ce-based material

As discussed in the previous paragraph, the understanding of the parameters that affect the stability within the blended OC material has a paramount importance to preserve the OC performances. To investigate these issues, a comparative study was conducted on redox-active CeO_2-based supports, focusing on the influence of adding structural promoters to CeO_2 relative to the pure oxide and $Ce_{0.8}Zr_{0.2}O_2$.

CeO_2 modified with 10 mol% Al_2O_3 or SiO_2 was synthesized via co-precipitation. Both Al_2O_3 and SiO_2 modifications are known to improve CeO_2 thermal stability and to facilitate oxygen vacancies formation and transport [39,40]. Fig. 5 shows the CH_4 conversion trends of composite samples realized by physically mixing C2F with Ni-impregnated supports: (i) CeO_2, (ii) $Ce_{0.8}Zr_{0.2}O_2$, (iii) CeO_2-Al_2O_3 and (iv) CeO_2-SiO_2. With the exception of the SiO_2-containing sample, all materials exhibited a comparable deactivation pattern. Among them, the composite with unmodified CeO_2 showed the most rapid deactivation, while the Al_2O_3-containing sample exhibited the slowest deactivation rate. In contrast, the Si-modified sample displayed a more stable behaviour, with a slight and gradual decline in CH_4 conversion over successive

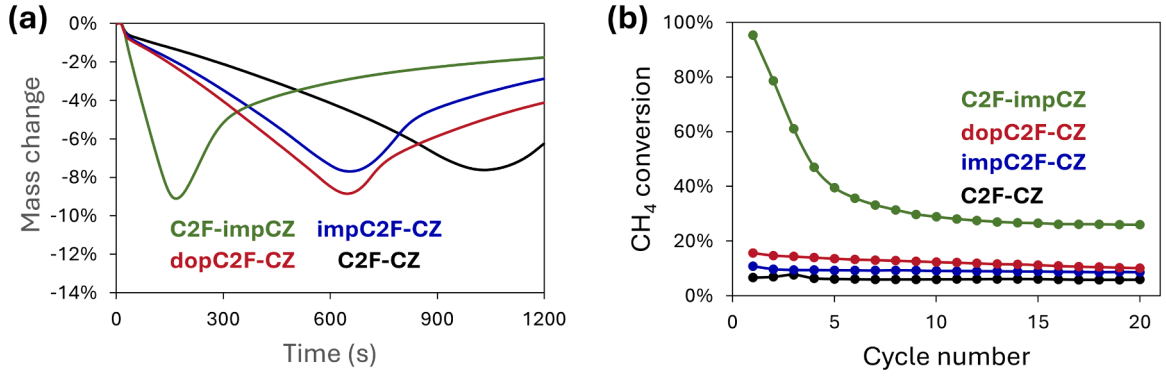

Fig. 3. (a) Relative mass variation of the composite samples upon isothermal reduction (5 % CH_4, 800 °C) in a TGA. (b) CH_4 conversion of composite samples in CL-SMR tests at 800 °C.

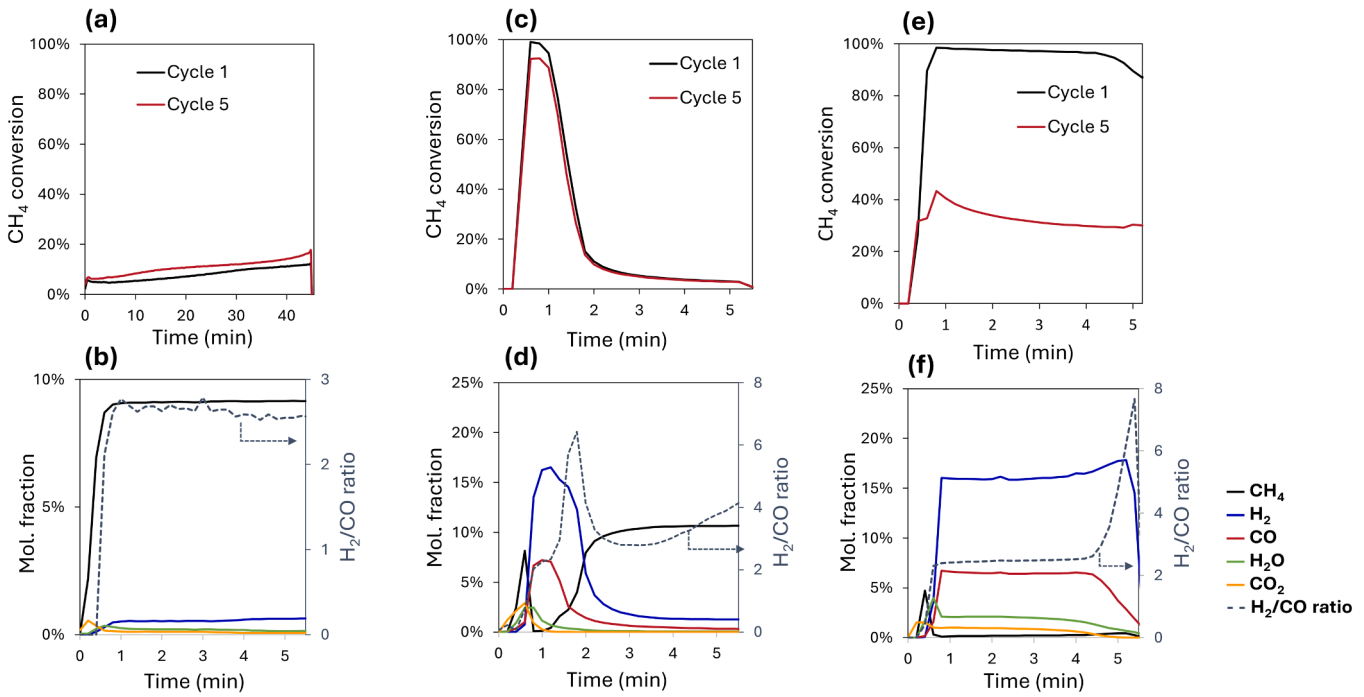

Fig. 4. CH_4 conversion and outlet gas profiles during the first reduction step of (a, b) $Ca_2Fe_2O_5$, (c, d) $Ni/Ce_{0.8}Zr_{0.2}O_2$ and (e, f) blended $Ca_2Fe_2O_5$ - $Ni/Ce_{0.8}Zr_{0.2}O_2$ during isothermal reduction at 800 °C.

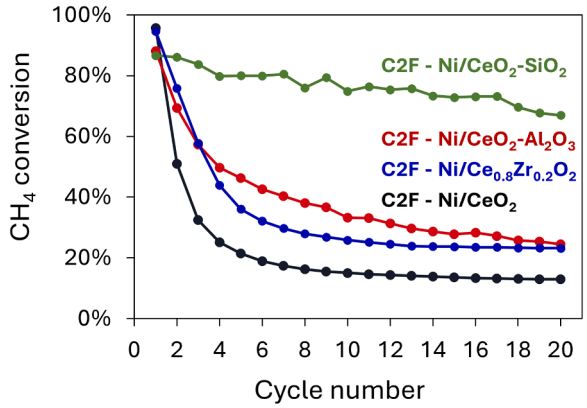

Fig. 5. CH_4 conversion of composite samples with different CeO_2-based components in CL-SMR tests at 800 °C.

cycles.

The tested samples were analysed using XRD, N_2 physisorption and SEM to investigate the structural and microstructural evolution that took place upon testing, with particular attention to the CeO_2-based component. While XRD analysis indicated that the crystalline structure remained largely unchanged (Figure S7), significant morphological changes were observed in the CeO_2-based materials due to redox cycling. All samples underwent a substantial decrease in surface area, which in the composite materials is primarily contributed by the CeO_2-based support (as shown in Table S1). This drop suggests considerable restructuring of the CeO_2 phase, which can be observed both from SEM imaging (Figure S8) and from the pore size distribution (Figure S9). Both techniques provide evidence that all modified samples have a significantly greater morphological stability than pure CeO_2. Of these samples, the SiO_2-modified material demonstrated the greatest retention of its original microstructure and porosity. These features are critical for stabilizing the active Ni particles decorated on the surface and preventing sintering and encapsulation within the support. Another important factor in determining active particles stability is provided by the strength of interaction with the support. Fig. 6 shows the H_2-TPR profiles of the Ni-loaded CeO_2-based materials. The total H_2 consumption is reported in Table S2. The reduction temperature of catalytic phase provides useful information about how the active phase interacts with the support. Specifically, low temperature contributions (150–300°C) correspond to the reduction of the bulk NiO that has no or weak interaction with CeO_2, while high temperature contributions (300–500 °C) represent the reduction of the NiO that has strong interaction with the support [41]. Ni/CeO_2 shows H_2 consumption between 120 and 300 °C, with a sharp peak at 210 °C. $Ni/Ce_{0.8}Zr_{0.2}O_2$ and Ni/CeO_2-SiO_2 exhibit similar features but shifted towards higher temperatures. $Ni/Ce_{0.8}Zr_{0.2}O_2$ shows H_2 consumption between 140 and 400 °C with a peak at 260 °C, while for Ni/CeO_2-SiO_2 the consumption takes place between 140 and 440 °C with a broad peak at 310 °C. Ni/CeO_2-Al_2O_3 shows a significantly lower total H_2 consumption, due to the inherent lower reducibility of the CeO_2-Al_2O_3 support (as shown in Figure S10). The profile evidences two distinct contributions, the first between 120 and 300 °C and the second between 320 and 500 °C. While the former can be attributed to weakly interacting Ni species [42], the

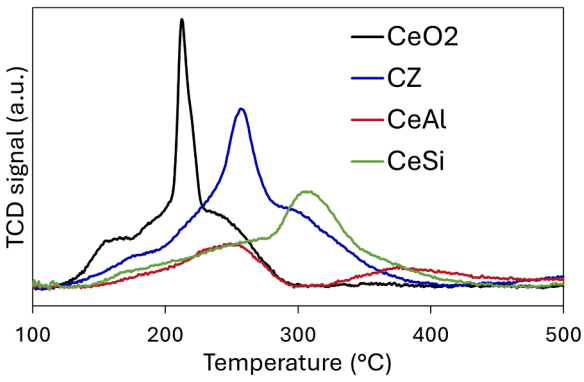

Fig. 6. H_2-TPR profiles of Ni-impregnated modified CeO_2 samples. Thermal Conductivity Detector (TCD) signal is expressed in arbitrary units (a.u.).

latter is associated with the reduction of Ni species in close contact with Al_2O [43]. The strong interaction of Ni with Al_2O_3 and the possible formation of poorly reducible mixed oxide phases with composition $NiAl_xO_y$ can significantly decrease Ni reducibility and catalytic activity [44–46].

Overall, our data indicate that Ni durability is influenced more by the support's morphology and the specific metal–support interaction than by the support's intrinsic redox properties. Supports that retain surface area and porosity during cycling, most notably SiO_2-modified ceria, and that form a moderate, non-encapsulating interaction with Ni preserve active-site dispersion and curb sintering, whereas structurally fragile supports or those that interact too strongly with Ni promote deactivation.

3.4. Insights on the chemistry and reactivity of $Ca_2F_2O_5$ - Ni/CeO_2-SiO_2

To elucidate the mechanisms underlying the stability of the C2F - Ni/CeO_2-SiO_2 composite, both solid-state chemical interactions between its constituents and gas-phase reactivity under different reactor configurations were systematically investigated.

3.4.1. Solid state interactions

To gain insight into the solid-state chemistry of Ni/CeO_2-SiO_2 - $Ca_2Fe_2O_5$ system during CL-SMR process, a series of *in situ* X-ray diffraction analysis were performed on the prepared OC material subjected to actual cycles. CO_2 was used as a substitute for H_2O to avoid issues with steam feeding and condensation. To both qualitatively and semi-quantitatively assess the phase transformations occurring during the redox cycles, two distinct structural indicators were monitored for each component of the blended OC material. Since CeO_2-based solid solutions are non-stoichiometric OCs, meaning that they can exchange oxygen by the reversible creation of lattice vacancies, CeO_2 reduction-oxidation process was tracked through the chemical expansion and contraction of its lattice induced by the generation of defect sites. In this sense, an increase of the lattice parameter is indicative of the formation of oxygen vacancies and of larger Ce^{3+} ions from Ce^{4+} [47]. Calcium and iron were found to be present as $Ca_2Fe_2O_5$, CaO, α-Fe and Fe_3C, respectively. The temporal evolution of these phases during redox cycling was monitored by tracking changes in the integrated intensity of a selected characteristic diffraction peak for each phase, which is approximately proportional to its abundance in the sample [48]. Powder Diffraction File (PDF) cards were used to index CeO_2 (01–075–0076), $Ca_2Fe_2O_5$ (01–071–2264), CaO (01–082–1691), α-Fe (00–001–1252) and Fe_3C (00–034–0001). The integrated peaks were chosen to be well-resolved and free from overlap with those pertaining to other phases. The temporal evolution of the interplanar distances (d spacing) is studied in each case. No Si-containing stable crystalline phases were observed. Silicon is therefore assumed to be present in the form of an amorphous SiO_2 matrix enveloping the CeO_2 crystallites, as reported in previous investigations [49]. Nonetheless, a partial incorporation of Si into the CeO_2 lattice, forming a $Ce_{1-x}Si_xO_2$ solid solution, cannot be ruled out. Reduction-oxidation cycles performed on the composite Ni/CeO_2-SiO_2 - $Ca_2Fe_2O_5$ sample revealed that the OC material undergoes reversible redox transitions between the initial (oxidized) state and a reduced state comprising oxygen-deficient $CeO_{2-\delta}$, CaO, and metallic Fe. Notably, Fe_3C formation was observed toward the end of the reduction phase, corresponding to the point where approximately 60–80 % of $Ca_2Fe_2O_5$ had been consumed. This carbide formation is attributed to methane pyrolysis and the subsequent diffusion of solid-state carbon into the metallic iron matrix. No carbonate phases, particularly $CaCO_3$, were detected during either the reduction or CO_2 oxidation steps, suggesting that carbonate formation is thermodynamically unfavoured under the tested conditions [50]. Analysis of the phase transformation kinetics (Fig. 7b,c) reveals a two-step mechanism for both reduction and oxidation. In the early stage of reduction, a rapid expansion of the CeO_2 lattice occurs, indicative of Ce^{4+} to Ce^{3+} reduction and oxygen vacancy formation. This is accompanied by a slower decomposition of $Ca_2Fe_2O_5$. After approximately 4 min, part of the metallic Fe is rapidly converted into Fe_3C. Concurrently, a fast additional lattice expansion is observed in CeO_2, likely driven by a localized increase in H_2 partial pressure resulting from CH_4 pyrolysis on Fe particles. During reoxidation, the initial step is marked by a gradual contraction of the CeO_2 lattice and the oxidation of Fe_3C back to metallic Fe. Once all Fe_3C is consumed, further oxidation leads to the simultaneous consumption of Fe and CaO and the reformation of $Ca_2Fe_2O_5$. The observation that $Ca_2Fe_2O_5$ only reforms once all iron is fully available supports the hypothesis that this is a single-step reaction mechanism, consistent with prior studies [51]. The reoxidation appears to reach completion shortly after exposure to 10 % CO_2, in line with thermodynamics and previous literature findings [18,52]. Subsequent cycles exhibited similar redox behaviour. To further assess the effect of different oxidizing agents, additional cycles were conducted using either CO_2 or O_2 alone as oxidizing agents. XRD patterns collected at the end of the oxidation steps (Figure S11) revealed no significant differences between the two treatments, suggesting that the choice of oxidant does not substantially alter the crystalline phase composition or induce phase segregation throughout the entire cycle. Overall, the composite material demonstrates excellent reversibility under conditions relevant to CL-SMR, along with a high degree of flexibility regarding the choice of oxidizing agent. More importantly, the results indicate that the two constituent phases can influence each other's reactivity through gas-phase reaction intermediates, as observed during the reduction step.

3.4.2. Gas phase interactions

In situ XRD measurements revealed that the two components do not chemically interact at the bulk level, suggesting that the large kinetic improvement is to be attributed to phenomena taking place in the gas phase. To investigate the interplay between C2F and the catalyst, equal amounts of C2F and Ni/CeO_2-SiO_2 were loaded into the reactor in a layered configuration and compared with the reference case in which the two powders were physically mixed prior to loading. The Ni/CeO_2-SiO_2 was positioned upstream of the C2F and separated from it by a quartz wool plug to prevent gas backmixing. Fig. 8 shows the measured CH_4 outlet gas fraction and the H_2/CO ratio during isothermal reduction at 800°C for the two cases. The initial CH_4 slip observed in both configurations is attributed to the low activity of NiO toward methane prior to its reduction to metallic Ni. In the layered bed configuration (Fig. 8a), significant carbon formation from CH_4 pyrolysis was observed immediately after the initial lag phase, as indicated by an increase in the H_2/CO ratio. This early carbon deposition inhibited the reactivity of the oxygen carrier (OC), limited oxygen exchange, and ultimately resulted in lower CH_4 conversion, as evidenced by the increase in the methane fraction at the reactor outlet. In contrast, when C2F and Ni/CeO_2-SiO_2 were co-located within the same reactive bed (Fig. 8b), the H_2/CO ratio remained stable at around 2 until around 3.5 min, after which it gradually increased toward the end of the step. CH_4 conversion was nearly complete throughout the entire period. The observed suppression of CH_4 pyrolysis in the mixed configuration is believed to result from interactions between the two components, mediated by locally evolved gas-phase reaction products. This mechanism is analogous to that proposed by More and Veser [22]. In brief, NiO is rapidly reduced by CH_4, forming metallic Ni, which catalyses CH_4 activation and its partial oxidation via lattice O^{2-} ions from the CeO_2 support [53]. The resulting H_2 and CO then locally promote the reduction of C2F, which proceeds more readily with these gases than with CH_4 alone [29]. The reduction of C2F in turn produces H_2O and CO_2, which are consumed by Ni-catalysed steam and dry methane reforming reactions and inhibits the formation of solid carbon on the active sites [54]. During the final stage of the reduction, large amounts of metallic iron are produced from the decomposition of C2F. This triggers the formation of Fe_3C (as observed during *in situ* XRD analysis) and increases the H_2/CO ratio. Overall, this cooperative mechanism between C2F and Ni/CeO_2-SiO_2

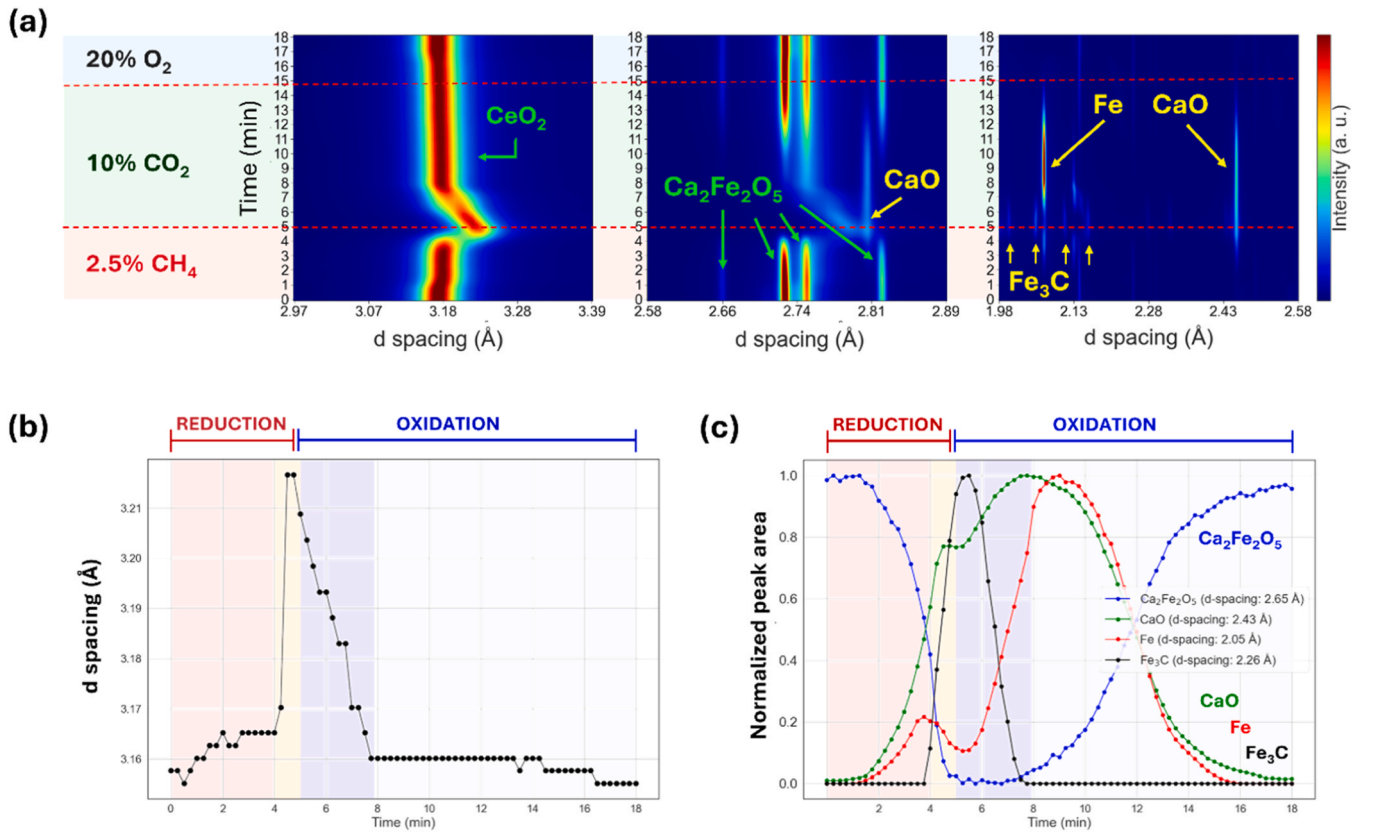

Fig. 7. (a) Time-resolved evolution of the main diffraction peaks corresponding to CeO_2, $Ca_2Fe_2O_5$, CaO, α-Fe and Fe_3C during the first CL-SMR cycle of the $Ca_2Fe_2O_5$ - Ni/CeO_2-SiO_2 composite sample. (b) Evolution over time of the d-spacing corresponding to the position of the main CeO_2 phase peak. (c) Idem for the area of peaks attributed to each crystalline phase.

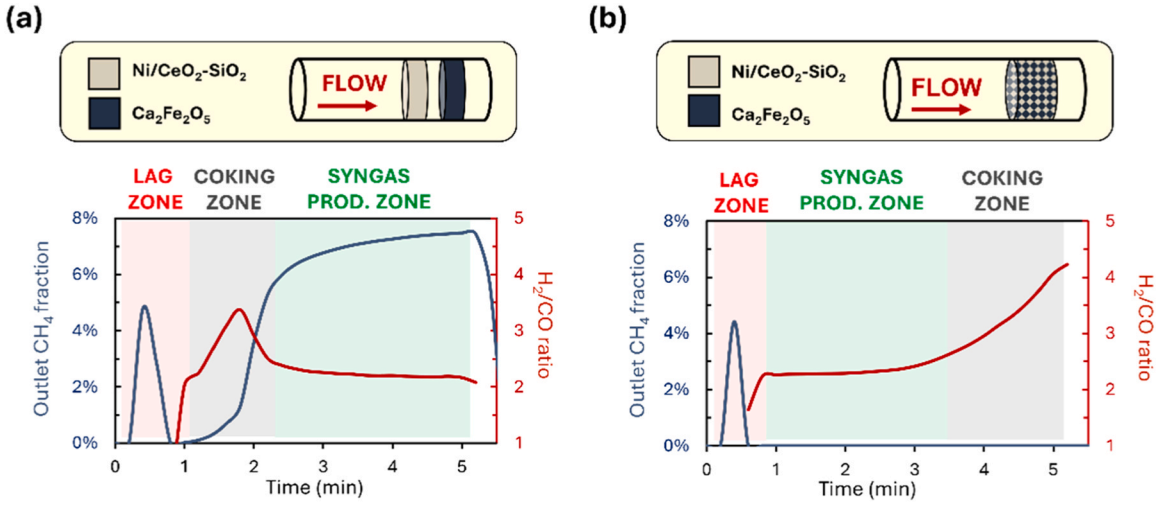

Fig. 8. CH_4 fraction and H_2/CO ratio measured at the reactor outlet during the first reduction step of (a) layered and (b) physically mixed $Ca_2Fe_2O_5$ - Ni/CeO_2-SiO_2 reactive bed.

enables a fast and continuous oxygen exchange, supporting a stable syngas generation and promoting the efficient use of the OC lattice oxygen.

3.4.3. *Role of oxygen*

In situ XRD analysis indicated that both C2F and CeO_2 are fully reoxidized by CO_2 (Fig. 7a). Given the comparable oxidizing potential of steam at the reaction temperature [55], it is expected that steam can likewise achieve complete oxidation of the two compounds. However, the analysis did not yield conclusive evidence regarding the oxidation state of Ni nanoparticles during the redox cycle. This limitation is attributed to the low Ni content in the composite, the small size of Ni particles, and the overlap of Ni and NiO diffraction peaks with those of the other crystalline phases present. Based on the reaction conditions, it is plausible that at least a fraction of the Ni is oxidized during the steam oxidation step. Nevertheless, it is unlikely that this involves bulk Ni structures or large nanoparticles [56]. In contrast, oxidation with O_2 can rapidly convert bulk Ni to NiO [57]. To assess the durability of the

oxygen carrier (OC) material under extended redox cycling, samples with a higher Ni loading (2.12 wt% on CeO_2-SiO_2) were prepared and subjected to 50 chemical looping steam methane reforming (CL-SMR) cycles. Additional experiments were conducted using H_2O as the sole oxidant to evaluate the specific role of the oxidation step in influencing the stability of the oxygen carrier. Fig. 9 show the CH_4 conversion trends for both conditions. The sample exposed to O_2 displayed stable performance after approximately 25–30 cycles, settling at approximately 90 % feed conversion. In contrast, the H_2O-only oxidized sample exhibited a marked decline in performance, with CH_4 conversion dropping to 30 % by the 45th cycle. Post-cycling XRD patterns (Figure S12) reveal significant structural differences between the two samples. The standard-cycled sample shows no signs of phase segregation, while Si-containing crystalline phases (quartz and Ca_2SiO_4) are detected in the H_2O-only sample, suggesting SiO_2 agglomeration and migration from CeO_2 to C2F. To investigate the accelerated deactivation observed under H_2O-only conditions, HAADF-STEM images were acquired before and after cycling. EDS mapping (Figures S13-S15) across all samples confirms a homogeneous distribution of Ca, Fe, Ce, and Si, indicating intimate contact between the C2F and the Ni/CeO_2-SiO_2 phases. Contrarily, Ni (shown in Fig. 10) appear clustered in some areas, suggesting its presence as individual nanoparticles. Ni particle growth is observed in both the tested samples relative to the pristine material. This is likely a consequence of the elevated reaction temperature and the presence of high concentrations of steam in the reactive gas, which is known to enhance the sintering of Ni particles [58,59]. Nevertheless, the average Ni domains size in the H_2O-only sample is more than twice that of the standard-cycled counterpart. Furthermore, co-localization of Ni and Fe is observed in the H_2O-only sample, which may indicate undesired migration and alloying. These findings suggest that periodic oxidation with O_2 plays a critical role in mitigating Ni sintering, likely through redispersion mechanisms triggered by redox cycling [60]. Therefore, incorporating an additional oxidation step using O_2 appears essential to sustain the high catalytic activity of Ni during prolonged operation.

Overall, the use of a suitable support (CeO_2-SiO_2) and an *in situ* regeneration strategy to maintain the catalytic activity of Ni (O_2-oxidation step) led to the development of a highly active and fairly stable OC material, able to obtain a syngas (H_2+CO) production of 13.4 mmol/g with high fuel conversion (88 %) and high CO selectivity (88 %) in the reduction step and 6.8 mmol/g of H_2 during the steam oxidation step. These values are in line with or superior to that reported for other OC systems, as shown in Table 2.

4. Conclusions and perspectives

The present contribution introduces a novel strategy to prepare Ni-promoted composite oxygen carriers for CL-SMR by the simple physical mixing of $Ca_2Fe_2O_5$ and modified CeO_2. The goal of developing such composite materials is to facilitate the efficient use of the available lattice oxygen and to enhance the reaction kinetics, particularly focusing on the reduction reaction. It is demonstrated that the spatial arrangement of Ni within the system could greatly affect the OC performances. At the microscale, direct chemical interactions between Fe and Ni are found to have a negative effect on reduction kinetics with CH_4. Because of that, the maximum utilization efficiency of the promoter is obtained when Ni is selectively deposited on the CeO_2-based material, with the latter acting as a physical barrier to prevent metals migrations and mixing/alloying. At the reactive bed scale, the co-localization of the two materials ($Ca_2Fe_2O_5$ and Ni/modified CeO_2), which comes by their physical mixing prior to reactor loading, is crucial to preserve the Ni active sites from coking, thanks to a synergistic gas phase-mediated mechanism that takes place between the components. A key factor to ensure a long-lasting promoting effect of Ni was found to be the morphological of the CeO_2-based material. The microstructure of the latter was found to be heavily affected by redox cycling when mixed with $Ca_2Fe_2O_5$. SiO_2-modified CeO_2 (10 % mol.) have shown a superior morphological stability and provided a higher Ni-support interaction, allowing for durable performance. Furthermore, it is shown that a short O_2-oxidation step at the end of each CL-SMR cycle can inhibit both Ni nanoparticles growth and the formation of undesired segregated phases, thus effectively representing a catalyst regeneration strategy.

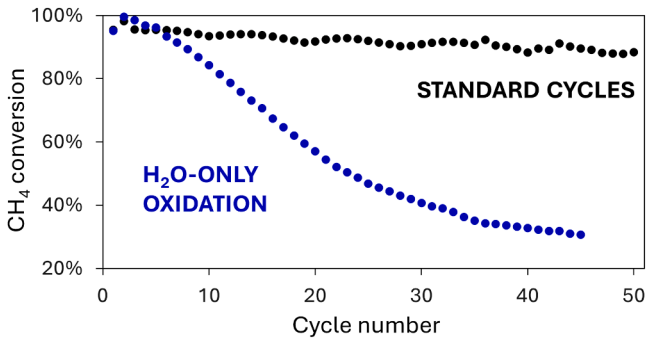

Fig. 9. CH_4 conversion obtained from Ni/CeO_2-SiO_2 - $Ca_2Fe_2O_5$ samples tested for 50 CL-SMR cycles with subsequent H_2O and O_2 oxidations (standard cycles), and H_2O-only cycles.

From these observations, it is inferred that the composite $Ca_2Fe_2O_5$ – Ni/CeO_2-SiO_2 OC material undergoes reduction by CH_4 producing H_2 and CO with a high selectivity and fast kinetics thanks to the complementary role of the supported Ni catalyst and the $Ca_2Fe_2O_5$. Oxidation with steam fully restores the $Ca_2Fe_2O_5$ and CeO_2 phases, while bulk Ni remains in its metallic form. Lastly, a short O_2 oxidation step at the end of the cycle ensures the reoxidation of bulk Ni, which is beneficial for the control of the metal particle size.

From application standpoint, the composite have to be thought as a functional package of oxides in which each component plays a synergistic role enabling CH_4 activation, selective lattice-oxygen transfer, and coke suppression. Co-optimization of the package formulation (relative amounts/dispersion of $Ca_2Fe_2O_5$, Ni and CeO_2–SiO_2) and of the redox operating conditions (temperature, CH_4/steam feed, extent and timing of O_2 regeneration) will be crucial to achieve continuous and stable syngas production with a tuneable H_2/CO ratio.

Industrial exploitation of these results will requires further studies addressing effective anti-sintering solutions and appropriate configurations for the CL reactor. In particular, a detailed sensitivity analysis is advised to clarify the relationship between the chemistry and microstructure of support and the anti-sintering properties. Moreover, targeted *operando* studies are recommended to map the optimal balance between steam and O_2 steps and thereby limit Ni ripening and Ni-Fe alloying.

Scale up will benefit from a co-current moving bed reducer which may promote synergy between gas phase and surface reactions and help maintain an oxidation-state gradient, thus ensuring high selectivity to syngas; this hypothesis should be validated through dedicated modelling and experimental campaigns. Moreover industrial application requires the development of engineered OC architectures (co-granulated or structured pellets) to ensure both co-localization of $Ca_2Fe_2O_5$ and Ni/CeO_2–SiO_2 and mechanical robustness under cyclic operation.

The insights gained from this study contribute to innovate the methodology to design new oxygen carriers and provide guidance for the rational development of low-cost, efficient, and stable materials for hydrocarbon-based chemical looping processes.

CRediT authorship contribution statement

Andrea Strazzolini: Writing – original draft, Visualization, Methodology, Investigation, Formal analysis, Data curation, Conceptualization. **Juan Felipe Basbus:** Writing – original draft. **Carla de Leitenburg:** Writing – review & editing, Supervision. **Jordi Llorca:** Writing – review & editing, Investigation. **Marta Boaro:** Writing –

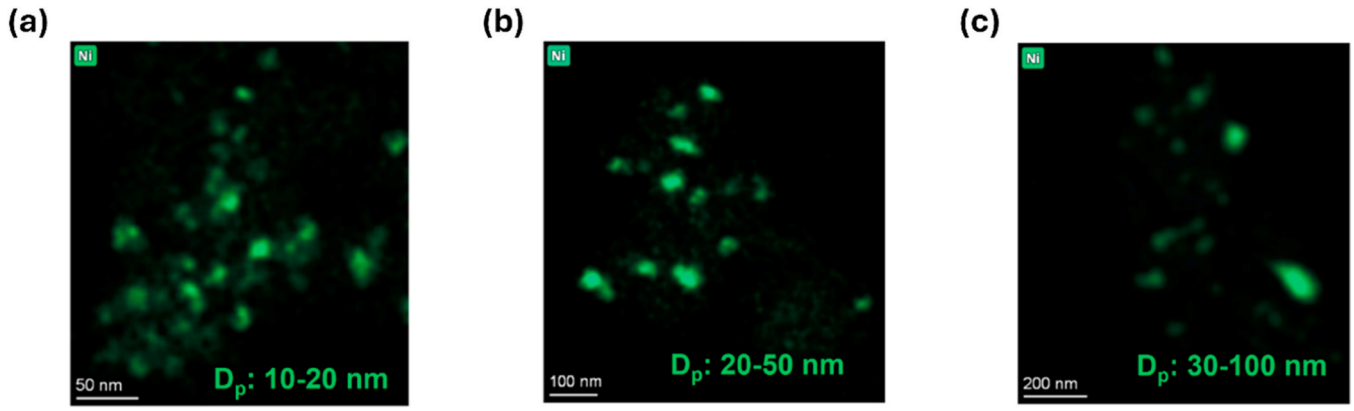

Fig. 10. Ni elemental maps acquired on the Ni/CeO_2-SiO_2 - $Ca_2Fe_2O_5$ sample (a) as prepared, (b) tested for 50 standard CL-SMR cycles and (c) tested for 45 H_2O-only cycles. The distribution of particles (D_p) is estimated in each case.

Table 2
Selected studies on CL-SMR from literature along with the present work, adapted from [61].

Oxygen carrier	Temperature (°C)	syngas yield (mmol/g)	CH_4 conv. (%)	H_2 yield (mmol/g)	H_2 purity (%)	Number of cycles	Ref.
$Ca_2Fe_2O_5$ - Ni/CeO_2-SiO_2	800	13.0	88	6.8	> 99	50	**This work**
$CuFe_2O_4$	900	9.3	54.5	11.3	> 99	5	[62]
3DOM $LaFe_{0.9}Ni_{0.1}O_3$	850	-	95	6.39	84.3	10	[63]
$La_{1.6}Sr_{0.4}FeCoO_6$	850	10.25	90	5.9	-	20	[64]
$BaCoO_3$/CeO_2	860	11.84	-	3.9	94.3	25	[65]
$Ce_{0.5}Fe_{0.5}O_{2-\delta}$	850	7.94	51	3.72	> 99	10	[66]
10 % CeO_2/3DOM $LaFeO_3$	800	9.94	-	3.38	> 99	30	[67]
$Ce_{0.8}Zr_{0.2}O_2$	800	-	55.89	1.88	-	10	[68]

review & editing, Supervision, Methodology, Funding acquisition, Conceptualization. **Trovarelli Alessandro:** Writing – review & editing, Resources.

Declaration of Competing Interest

The authors declare that they have no known competing financial interests or personal relationships that could have appeared to influence the work reported in this paper.

Acknowledgements

A. S. acknowledges the financial support of the Italian Ministry of University and Research (MUR) through a Ph.D. fellowship under the XXXVII doctoral cycle.

The authors thank to BL04 MSPD beamline, ALBA Synchrotron, Consortium for the Construction, Equipping and Exploitation of the Synchrotron Light Source (CELLS) and experimental staff during XRD measurements.

The research has been funded within the Program ex DM 737/2021 financially supported by the European Union, - NextGenerationEU.

J.L. is a Serra Húnter Fellow and is grateful to the Maria de Maeztu Units of Excellence Programme CEX2023-001300-M funded by MCIN/AEI 10.13039/501100011033 and project MICIU/FEDER PID2024-156765OB-C21. HAADF-STEM-EDS was performed at the Joint Electron Microscopy Center (JEMCA) at ALBA Synchrotron with the collaboration of ALBA staff.

Appendix A. Supporting information

Supplementary data associated with this article can be found in the online version at doi:10.1016/j.apcatb.2025.126037.

Data availability

Data will be made available on request.

References

[1] International Energy Agency, World Energy Outlook 2022, IEA, Paris, 2022 https://www.iea.org/reports/world-energy-outlook-2022.
[2] J.O. Ighalo, P.B. Amama, Recent advances in the catalysis of steam reforming of methane (SRM), Int. J. Hydrog. Energy 51 (2024) 688–700.
[3] M. Bachmann, S. Völker, J. Kleinekorte, A. Bardow, Syngas from what? Comparative life-cycle assessment for syngas production from biomass, CO_2, and steel mill off-gases, ACS Sustain. Chem. Eng. 11 (2023) 5356–5366.
[4] H. Zheng, X. Jiang, Y. Gao, A. Tong, L. Zeng, Chemical looping reforming: process fundamentals and oxygen carriers, Discov. Chem. Eng. 2 (2022) 5.
[5] V. Spallina, B. Marinello, F. Gallucci, M.C. Romano, M. Van Sint Annaland, Chemical looping reforming in packed-bed reactors: modelling, experimental validation and large-scale reactor design, Fuel Process. Technol. 156 (2017) 156–170.
[6] Q. Zhou, L. Zeng, L. Fan, Syngas chemical looping process: dynamic modelling of a moving-bed reducer, AIChE J. 59 (2013) 3432–3443.
[7] G. Voitic, V. Hacker, Recent advancements in chemical looping water splitting for the production of hydrogen, RSC Adv. 6 (2016) 98267–98296.
[8] K. Svoboda, G. Slowinski, J. Rogut, D. Baxter, Thermodynamic possibilities and constraints for pure hydrogen production by iron-based chemical looping at lower temperatures, Energy Convers. Manag 48 (2007) 3063–3073.
[9] Z. Yu, Y. Yang, S. Yang, Q. Zhang, J. Zhao, Y. Fang, et al., Iron-based oxygen carriers in chemical looping conversions: a review, Carbon Resour. Convers. 2 (2019) 23–34.
[10] K. Zhao, F. He, Z. Huang, G. Wei, A. Zheng, H. Li, et al., Perovskite-type oxides $LaFe_{1-x}Co_xO_3$ for chemical looping steam methane reforming to syngas and hydrogen co-production, Appl. Energy 168 (2016) 193–203.
[11] Y. Kang, Y. Han, M. Tian, C. Huang, C. Wang, J. Lin, et al., Promoted methane conversion to syngas over Fe-based garnets via chemical looping, Appl. Catal. B 278 (2020) 119305.
[12] K. Zhao, F. He, Z. Huang, A. Zheng, H. Li, Z. Zhao, Three-dimensionally ordered macroporous $LaFeO_3$ perovskites for chemical looping steam reforming of methane, Int. J. Hydrog. Energy 39 (2014) 3243–3252.
[13] D. Zeng, D. Cui, Y. Qiu, M. Li, L. Ma, S. Zhang, et al., Mn-Fe-Al-O mixed spinel oxides as oxygen carriers for chemical looping hydrogen production with CO_2 capture, Fuel 274 (2020) 117854.

[14] S. Sun, M. Zhao, L. Cai, S. Zhang, D. Zeng, R. Xiao, Performance of CeO_2-modified iron-based oxygen carrier in chemical looping hydrogen generation, Energy Fuels 29 (2015) 7612–7621.

[15] M. Ismail, W. Liu, D.M.T. Dunstan, S.A. Scott, Development and performance of iron-based oxygen carriers containing calcium ferrites for chemical looping combustion and hydrogen production, Int. J. Hydrog. Energy 41 (2016) 4073–4084.

[16] W. Liu, L. Shen, H. Gu, L. Wu, Chemical looping hydrogen generation using potassium-modified iron ore as an oxygen carrier, Energy Fuels 30 (2016) 1756–1763.

[17] A. Shaula, Y. Pivak, J. Waerenborgh, P. Gaczynski, A. Yaremchenko, V. Kharton, Ionic conductivity of brownmillerite-type calcium ferrite under oxidizing conditions, Solid State Ion. 177 (2006) 2923–2930.

[18] V. Shah, Z. Cheng, D.S. Baser, J.A. Fan, L.S. Fan, Highly selective production of syngas from chemical looping reforming of methane with CO_2 utilization on MgO-supported calcium ferrite redox materials, Appl. Energy 282 (2021) 116111.

[19] L. Wang, Y. Lin, Z. Huang, K. Zeng, H. Huang, Conversion of carbon dioxide to carbon monoxide: two-step chemical looping dry reforming using $Ca_2Fe_2O_5$–$Zr_{0.5}Ce_{0.5}O_2$ composite oxygen carriers, Fuel 322 (2022) 124182.

[20] D. Hosseini, F. Donat, P.M. Abdala, S.M. Kim, A.M. Kierzkowska, C.R. Müller, Reversible exsolution of dopant improves the performance of $Ca_2Fe_2O_5$ for chemical looping hydrogen production, ACS Appl. Mater. Interfaces 11 (2019) 18276–18285.

[21] S. Zhang, X. Guo, Co, ni and Cu-doped $Ca_2Fe_2O_5$-based oxygen carriers for enhanced chemical looping hydrogen production, J. Energy Inst. 114 (2024) 101659.

[22] A. More, G. Veser, Physical mixtures as simple and efficient alternative to alloy carriers in chemical looping processes, AIChE J. 63 (2017) 51–59.

[23] M.A. Pans, P. Gayán, A. Abad, F. García-Labiano, L.F. de Diego, J. Adánez, Use of chemically and physically mixed iron and nickel oxides as oxygen carriers for gas combustion in a CLC process, Fuel Process. Technol. 115 (2013) 152–163.

[24] J. Hu, V.V. Galvita, H. Poelman, C. Detavernier, G.B. Marin, Catalyst-assisted chemical looping auto-thermal dry reforming: spatial structuring effects on process efficiency, Appl. Catal. B 231 (2018) 123–136.

[25] M. Ismail, W. Liu, M.S.C. Chan, D.M.T. Dunstan, S.A. Scott, Synthesis, application and carbonation behavior of $Ca_2Fe_2O_5$ for chemical looping H_2 production, Energy Fuels 30 (2016) 6220–6229.

[26] A. Pappacena, K. Schermanz, A. Sagar, E. Aneggi, T. Trovarelli, Development of a modified co-precipitation route for thermally resistant, high-surface-area ceria–zirconia solid solutions, Mater. Res. Soc. Symp. Proc. (2010) 835–838.

[27] K. Okada, T. Tomita, Y. Kameshima, A. Yasumori, K.J.D. MacKenzie, Porous properties of co-precipitated Al_2O_3–SiO_2 xerogels prepared from aluminium nitrate nonahydrate and tetraethylorthosilicate, J. Mater. Chem. 9 (1999) 1307–1312.

[28] Y. Zou, H. Liu, R. Li, J. Liu, C. Wu, Z. Sun, et al., Ni/Al co-doping induces FeO_6 octahedral distortion to activate lattice oxygen in $Ca_2Fe_2O_5$ for enhanced chemical looping hydrogen generation, J. Mater. Chem. A 13 (2025) 21601–21614.

[29] M.S. Sukma, Y. Zheng, P. Hodgson, S.A. Scott, Understanding the behavior of dicalcium ferrite ($Ca_2Fe_2O_5$) in chemical looping syngas production from CH_4, Energy Fuels 36 (2022) 9410–9422.

[30] S. Sun, S. He, C. Wu, Ni-promoted Fe–CaO dual functional materials for calcium chemical dual looping, Chem. Eng. J. 441 (2022) 135752.

[31] J. Huang, W. Liu, Y. Yang, B. Liu, High-performance Ni–Fe redox catalysts for selective CH_4 to syngas conversion via chemical looping, ACS Catal. 8 (2018) 1748–1756.

[32] T. Xu, X. Wang, H. Zhao, B. Xiao, D. Liu, W. Liu, Modulating lattice oxygen activity of $Ca_2Fe_2O_5$ brownmillerite for co-production of syngas and high-purity H_2 via chemical looping steam reforming of toluene, Appl. Catal. B 320 (2023) 122010.

[33] A. Trovarelli, Structural and oxygen storage/release properties of CeO_2-based solid solutions, Comments Inorg. Chem. 20 (1999) 263–284.

[34] D.G. Araiza, A. Gómez-Cortés, G. Díaz, Effect of ceria morphology on carbon deposition during steam reforming of ethanol over Ni/CeO_2 catalysts, Catal. Today 349 (2020) 235–243.

[35] K. Tang, W. Liu, J. Li, J. Guo, J. Zhang, S. Wang, et al., Effect of exposed facets of ceria to the nickel species in nickel-ceria catalysts and their performance in a NO + CO reaction, ACS Appl. Mater. Interfaces 7 (2015) 26839–26849.

[36] G. Tang, J. Gu, G. Wei, H. Yuan, Y. Chen, Reaction performance and mechanism of a NiO/$Ca_2Fe_2O_5$ oxygen carrier in chemical looping gasification of cellulose, Chem. Eng. J. 451 (2023) 137516.

[37] Y. Zheng, M.S. Sukma, S.A. Scott, Exploration of NiO/$Ca_2Fe_2O_5$/CaO in chemical looping methane conversion for syngas and H_2 production, Chem. Eng. J. 465 (2023) 142779.

[38] A. Strazzolini, R. Ramezani, G. de Felice, L. di Felice, C. de Leitenburg, A. Trovarelli, et al., High-pressure reduction kinetics of $Ca_2Fe_2O_5$ for advanced chemical looping steam reforming, Ind. Eng. Chem. Res. 64 (2025) 9914–9924.

[39] M. Pijolat, M. Prin, M. Soustelle, O. Touret, P. Nortier, Thermal stability of doped ceria: experiment and modelling, J. Chem. soc, Faraday Trans. 91 (1995) 3941–3946.

[40] E. Rocchini, T. Trovarelli, J. Llorca, G.W. Graham, W.H. Weber, M. Maciejewski, et al., Relationships between structural/morphological modifications and oxygen storage–redox behavior of silica-doped ceria, J. Catal. 194 (2000) 461–478.

[41] Y. Ma, J. Liu, M. Chu, J. Yue, Y. Cui, G. Xu, Enhanced low-temperature activity of CO_2 methanation over Ni/CeO_2 catalyst, Catal. Lett. 152 (2022) 872–882.

[42] I. Luisetto, S. Tuti, C. Battocchio, S. Lo Mastro, A. Sodo, Ni/CeO_2–Al_2O_3 catalysts for dry reforming of methane: effect of $CeAlO_3$ content and ni crystallite size on activity and coke resistance, Appl. Catal. A 500 (2015) 12–22.

[43] S. Sangsong, T. Ratana, S. Tungkamani, T. Sornchamni, M. Phongaksorn, Effect of CeO_2 loading of Ce–Al mixed oxide on ultrahigh-temperature water-gas shift over ni catalysts, Fuel 252 (2019) 488–495.

[44] Y. Zhang, G. Xiong, S. Sheng, W. Yang, Deactivation studies over NiO/γ-Al_2O_3 catalysts for partial oxidation of methane to syngas, Catal. Today 63 (2000) 517–522.

[45] C. Li, Y.W. Chen, Temperature-programmed reduction studies of nickel oxide/alumina catalysts: effects of preparation method, Thermochim. Acta 256 (1995) 457–465.

[46] C. Dueso, A. Abad, F. García-Labiano, L.F. de Diego, P. Gayán, J. Adánez, et al., Reactivity of a NiO/Al_2O_3 oxygen carrier prepared by impregnation for chemical-looping combustion, Fuel 89 (2010) 3399–3409.

[47] D. Marrocchelli, S.R. Bishop, H.L. Tuller, B. Yildiz, Understanding chemical expansion in non-stoichiometric oxides: ceria and zirconia case studies, Adv. Funct. Mater. 22 (2012) 1958–1965.

[48] B.D. Cullity, S.R. Stock, Elements of X-ray Diffraction, Prentice-Hall, Upper Saddle River, 2001.

[49] H.T.T. Nguyen, M. Ohtani, K. Kobiro, One-pot synthesis of SiO_2–CeO_2 nanoparticle composites with enhanced heat tolerance, Microporous Mesoporous Mater. 273 (2019) 35–40.

[50] M.V. Iyer, H. Gupta, B.B. Sakadjian, L.S. Fan, Multicyclic study on the simultaneous carbonation and sulfation of high-reactivity CaO, Ind. Eng. Chem. Res. 43 (2004) 3939–3947.

[51] D.D. Miller, J. Riley, R. Siriwardane, Interaction of methane with calcium ferrite in chemical looping partial oxidation: experimental and DFT study, Energy Fuels 34 (2020) 2193–2204.

[52] A. Löfberg, J. Guerrero-Caballero, T. Kane, A. Rubbens, L. Jalowiecki-Duhamel, Ni/CeO_2-based catalysts as oxygen vectors for chemical looping dry reforming of methane for syngas production, appl. Catal. b 212 (2017) 159–174.

[53] Y. Han, M. Tian, C. Wang, Y. Kang, L. Kang, Y. Su, et al., Highly active and anticoke Ni/CeO_2 with ultralow ni loading in chemical looping dry reforming via strong metal–support interaction, ACS Sustain. Chem. Eng. 9 (2021) 17276–17288.

[54] D. Pashchenko, I. Makarov, Carbon deposition in steam methane reforming over a Ni-based catalyst: experimental and thermodynamic analysis, Energy 222 (2021) 119993.

[55] X. Zhu, Q. Imtiaz, F. Donat, C.R. Müller, F. Li, Chemical looping beyond combustion – a perspective, Energy Environ. Sci. 13 (2020) 772–804, https://doi.org/10.1039/C9EE02943K.

[56] M. Wolf, Thermodynamic assessment of bulk and nanoparticulate cobalt and nickel stability during dry and steam reforming of methane, RSC Adv. 11 (2021) 18187–18197.

[57] R. You, Y. Ou, R. Qi, J. Yu, F. Wang, Y. Jiang, et al., Revealing temperature-dependent oxidation dynamics of ni nanoparticles via ambient-pressure TEM, Nano Lett. 23 (2023) 7260.

[58] D.H. Prasad, S.Y. Park, H. Ji, H.R. Kim, J.W. Son, B.K. Kim, et al., Effect of steam content on nickel nanoparticle sintering and methane reforming activity of Ni–CZO anode cermets for internal-reforming SOFCs, Appl. Catal. A 411–412 (2012) 160–169.

[59] J. Sehested, Sintering of nickel steam-reforming catalysts: effects of temperature and steam and hydrogen pressures, J. Catal. 223 (2004) 432–443.

[60] O. Kwon, A.C. Foucher, R. Huang, E.A. Stach, J.M. Vohs, R.J. Gorte, Evidence for redispersion of Ni on $LaMnO_3$ films following high-temperature oxidation, J. Catal. 407 (2022) 213–220.

[61] S. Das, A. Biswas, C.S. Tiwary, M. Paliwal, Hydrogen production using chemical looping technology: a review with emphasis on H_2 yield of various oxygen carriers, Int. J. Hydrog. Energy 47 (2022) 28322–28352.

[62] K.S. Kang, C.H. Kim, W.C. Cho, K.K. Bae, S.W. Woo, C.S. Park, Reduction characteristics of $CuFe_2O_4$ and Fe_3O_4 by methane; $CuFe_2O_4$ as an oxidant for two-step thermochemical methane reforming, Int. J. Hydrog. Energy 33 (2008) 4560–4568.

[63] Y. Shen, K. Zhao, F. He, H. Li, Structure–reactivity relationships of 3-dimensionally ordered macroporous $LaFe_{1-x}Ni_xO_3$ perovskites for chemical looping steam methane reforming, J. Energy Inst. 92 (2019) 239–246.

[64] K. Zhao, L. Li, A. Zheng, Z. Huang, F. He, Y. Shen, et al., Synergistic improvements in stability and performance of double perovskite $La_{2-x}Sr_xFeCoO_6$ for chemical looping steam methane reforming, Appl. Energy 197 (2017) 393–404.

[65] H. Ding, Y. Xu, C. Luo, Q. Wang, C. Shen, J. Xu, et al., Composite perovskite-based material for chemical looping steam methane reforming to hydrogen and syngas, Energy Convers. Manag 171 (2018) 12–19.

[66] X. Zhu, Y. Wei, H. Wang, K. Li, Ce–Fe oxygen carriers for chemical looping steam methane reforming, Int. J. Hydrog. Energy 38 (2013) 4492–4501.

[67] Y. Zheng, K. Li, H. Wang, D. Tian, Y. Wang, X. Zhu, et al., Designed oxygen carriers from macroporous $LaFeO_3$-supported CeO_2 for chemical looping reforming of methane, Appl. Catal. B 202 (2017) 51–63.

[68] Y. Zheng, Y. Wei, K. Li, X. Zhu, H. Wang, Y. Wang, Chemical looping steam methane reforming over macroporous CeO_2–ZrO_2 solid solution: effect of calcination temperature, Int. J. Hydrog. Energy 39 (2014) 13361–13368.